



Convolutional restricted Boltzmann machine correlated variational wave function for the Hubbard model on a square lattice

Karthik V. ^{*} and Amal Medhi [†]*Indian Institute of Science Education and Research Thiruvananthapuram, Kerala 695551, India*

(Received 6 February 2024; accepted 28 August 2024; published 11 September 2024)

We use a convolutional restricted Boltzmann machine (CRBM) neural network to construct a variational wave function (WF) for the Hubbard model on a square lattice and study it using the variational Monte Carlo (VMC) method. In the wave function, the CRBM acts as a correlation factor to a mean-field BCS state. The number of variational parameters in the WF does not grow automatically with the lattice size and it is computationally much more efficient compared with other neural-network-based WFs. We find that, in the intermediate- to strong-coupling regime of the model at half filling, the wave function outperforms even the highly accurate long-range backflow-Jastrow correlated wave function. Using the WF, we study the ground state of the half filled model as a function of onsite Coulomb repulsion U . We consider two cases for the next-nearest-neighbor hopping parameter, e.g., $t' = 0$ as well as a frustrated model case with $t' \neq 0$. By examining several quantities, e.g., double occupancy, charge gap, momentum distribution, and spin-spin correlations, we find that the weakly correlated phase in both cases is paramagnetic metallic (PM). As U is increased, the system undergoes a first-order Mott transition to an insulating state at a critical U_c , the value of which depends on t' . The Mott state in both cases is spin gapped with long-range antiferromagnetic (AFM) order. Remarkably, the AFM order emerges spontaneously from the wave function which does not have any explicitly broken symmetry in it. Apart from some quantitative differences in the results for the two values of t' , we find some interesting qualitative differences in the way the Mott transition takes place in the two cases.

DOI: [10.1103/PhysRevB.110.125125](https://doi.org/10.1103/PhysRevB.110.125125)

I. INTRODUCTION

The Hubbard Hamiltonian has been studied extensively over the years using a variety of analytical and numerical methods as a paradigmatic model for various correlated electron phenomena [1,2]. The model on a two-dimensional lattice is particularly interesting because of its relevance to the high-temperature superconductors [3]. Theoretically, the model is handled well both in the weak and strong-coupling limits by different methods, but not so in the most interesting intermediate-coupling regime. Among various numerical methods, the variational Monte Carlo (VMC) technique has been a very useful over the years in the study of the ground-state properties of the model and its various extensions [4–8]. Unlike other methods, VMC does not suffer from any particular difficulty at any coupling strength, but its results are always biased by the choice of the variational wave function (WF), which is generally constructed based on the ground state of an underlying mean-field Hamiltonian. However, with the advent of machine-learning algorithms based on artificial neural networks (ANNs), it was realized that ANNs can also be used to represent a quantum many-body wave function [9–14]. In such wave functions termed as neural-network quantum states (NQS), the number of variational degrees of freedom is large and it offers the possibility to overcome the fundamental

limitation of the variational method by enabling the construction of a highly unbiased variational wave function.

A number of seminal works have already demonstrated the power of NQS to learn quantum many-body physics [13,15–18]. To mention some of these, Carleo and Troyer [10] first demonstrated the use of a restricted Boltzmann machine-based (RBM-based) variational wave function to represent the ground state and study the dynamics of a few prototypical spin Hamiltonians accurately and efficiently. The method involved training the network by using a reinforcement learning mechanism which essentially is an iterative tuning of the network parameters so as to minimize the variational energy. Torlai *et al.* [19] used an NQS wave function based on an RBM network to perform a quantum state tomography and thereby learn the ground state of a quantum spin Hamiltonian. In Ref. [20], the authors used a wave function based on deep Boltzmann machine (DBM) and performed imaginary time evolution to obtain accurate ground state of the transverse-field Ising and the Heisenberg model. Choo *et al.* [21], by incorporating translational symmetries explicitly into the NQS wave function, managed to generate also the excited states for the Heisenberg and Bose-Hubbard models. RBM were also shown to be very efficient in representing topological quantum states due to the nonlocal geometry of its architecture [22,23]. However, most of these applications so far have been to bosonic systems. One main reason for this is that the fermionic systems have an additional complexity that comes from the nontrivial sign structures of its wave functions [24]. The functions that can be represented

^{*}Contact author: karthik.v16@iisertvm.ac.in[†]Contact author: amedhi@iisertvm.ac.in

by neural-networks though highly nonlinear are essentially smooth and generally fail to represent the sign structures of fermionic many-body wave functions. For instance, the feed-forward neural networks, a type of ANN, were shown to be unable to correctly account for the sign structure of even a free fermionic wave function [25]. Nomura *et al.* [26] constructed a wave function by combining an RBM with a mean-field part where the RBM part introduces correlation effects, a role usually played by Jastrow-type correlation factors [6]. It was shown that the combination wave function give substantially lower energy than the conventional projected variational wave functions for the fermionic Hubbard model as well as the Heisenberg model. There also exist other scheme-based ANNs for fermionic systems, but these are restricted to small system size due to computational complexity [27–30].

In this work, we construct a ground-state variational wave function for the fermionic Hubbard model on a square lattice using a convolutional restricted Boltzmann machine (CRBM) network where the CRBM is used as a correlation factor to a mean-field BCS state. We show that the wave function is not only computationally efficient compared with the RBM wave function, it is also highly accurate in terms of the variational energy. Using VMC, we study the wave function as a ground state of the model at half filling as a function of onsite Coulomb repulsion U . We consider two cases of the model when the next-nearest-neighbor hopping parameter $t' = 0$ and when the model is frustrated with $t' \neq 0$. The wave function yields energies which are significantly lower compared with those of the corresponding RBM or Jastrow-projected wave functions, especially in the strong-coupling limit. Indeed, in this limit it outperforms in terms of energy even the highly accurate long-range backflow-Jastrow correlated wave function for the model. The wave function correctly captures the presence of doublon-holon (DH) binding in the strong-coupling regime in spite of it having no explicit DH binding term. It also give rise to long-range antiferromagnetic (AFM) order in the Mott insulating state spontaneously even though the wave function contains no explicit magnetic order. We examine the nature of Mott metal-insulator transition in the model by calculating various quantities, such as double occupancy, charge gap, momentum distribution and quasiparticle weight, and spin-spin correlation. The results are thoroughly discussed and compared with other variational results.

The rest of the paper is organized as follows: In Sec. II, we describe the model and the CRBM wave function. In Sec. III, we describe and discuss the results, and finally in Sec. IV, we make the concluding remarks.

II. MODEL AND METHOD

We consider the fermionic Hubbard model on a two-dimensional (2D) square lattice at half filling. The Hamiltonian is given by

$$\mathcal{H} = - \sum_{i,j\sigma} t_{ij} (c_{i\sigma}^\dagger c_{j\sigma} + hc) + U \sum_i n_{i\uparrow} n_{i\downarrow}, \quad (1)$$

where the operator $c_{i\sigma}^\dagger$ creates an electron at site “ i ” with spin σ . $c_{i\sigma}$ is the corresponding annihilation operator and $n_{i\sigma} = c_{i\sigma}^\dagger c_{i\sigma}$ is the number operator. The first term represents

hoppings of electrons from site to site. The hopping integrals are $t_{ij} = t$ for i, j nearest-neighbor (NN) sites, $t_{ij} = -t'$ for i, j next-nearest-neighbor (NNN) sites, and zero otherwise. Due to the particle-hole symmetry at half filling, the model is equivalent to the case with opposite sign of t' . The Hamiltonian is the simplest paradigmatic model that capture the essential physics of several interesting correlated electron phenomenon in condensed-matter physics, including the Mott metal-insulator transition, high-temperature cuprate superconductors, etc [1,3,31,32]. The Mott physics in the Hubbard model has been studied extensively using various methods [33–42], including variational theory within the framework of various Gutzwiller-Jastrow type wave functions (WFs) [43–48]. These projected variational wave functions are typically of the form, $|\Psi_{\text{var}}\rangle = \mathcal{P}|\Phi\rangle$, where $|\Phi\rangle$ is a one-body wave function which is generally taken to be ground state of an underlying mean-field Hamiltonian. \mathcal{P} is a projection operator or correlation factor which introduces many-body correlation into the wave function. The simplest case is the Gutzwiller (GW) projector \mathcal{P}_G which describes an on-site density-density correlation, $\mathcal{P}_G = \prod_i [1 - (1-g)n_{i\uparrow}n_{i\downarrow}]$, $0 < g \leq 1$. It penalizes electronic configurations with doubly occupied sites thereby giving a better description of the ground state of the Hubbard model compared with the uncorrelated state. However, GW projector was found to be inadequate to describe the Mott insulating state. This is because in the Mott state, local charge fluctuations creates configurations with doubly occupied sites (doublons) next to empty sites (holons). The insulating nature of the state means that the doublons and holons must be bound to each other and the GW projector does not capture this effect [44–46,49]. It was shown that the situation can be greatly improved by considering a correlation factor of the form $\mathcal{P} = \mathcal{P}_{DH}\mathcal{P}_G$, where the factor \mathcal{P}_{DH} incorporates doublon-holon (DH) binding in the wave function and is given by [44], $\mathcal{P}_{DH} = \prod_i (1 - \eta Q_i)$, with $Q_i = \prod_\delta [d_i(1 - h_{i+\delta}) + h_i(1 + d_{i+\delta})]$. Here $d_i = n_{i\uparrow}n_{i\downarrow}$ is doublon and $h_i = (1 - n_{i\uparrow})(1 - n_{i\downarrow})$ is holon operator, δ denotes the nearest-neighbor sites, and η is a variational parameter. Alternatively, one can also consider Jastrow factor of the form [45] $\mathcal{P}_J = \exp[\sum_{ij} \frac{1}{2} v_{ij} (n_i - 1)(n_j - 1) + w_{ij} h_i d_j]$ which introduces long-range correlations including DH binding. The description can be further improved by introducing a backflow correlation term in addition to the Jastrow factor and such a wave function considered for the half filled Hubbard model was shown to be much better in terms of the ground-state energy and in the description of the Mott insulating state in the model [48].

Here, we consider a variational wave function where the correlator is based on an artificial neural-network (ANN). Such a wave function using the restricted Boltzmann machine (RBM) network as a correlator was already considered for the Hubbard as well as the Heisenberg model [26]. Here we consider a convolutional restricted Boltzmann machine (CRBM) network as a correlator. The CRBM is computationally much more efficient than an RBM owing to much lesser number of network connections and consequently fewer number of variational parameters in CRBM. In fact, the number of variational parameters in CRBM can be tuned and does not grow automatically with the lattice size which is a highly desirable feature computationally. In the followings, first we describe

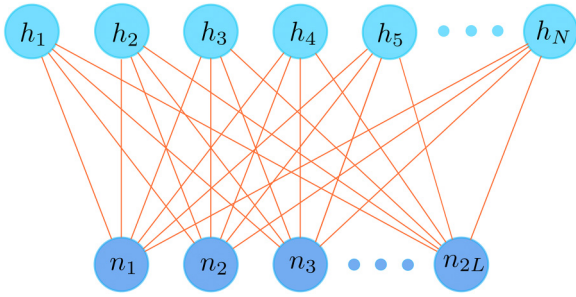


FIG. 1. A restricted Boltzmann machine (RBM) network. The artificial neurons in the visible layer take the inputs $\{n_1, n_2, \dots, n_{2L}\}$ that represent the sets of electron occupation numbers. The neurons in the hidden layer define variables h_i which can take values ± 1 .

the RBM network followed by a detailed description of the structure of the CRBM network. The variational wave function using the CRBM as a correlator is described next.

A. Restricted Boltzmann machine network

A restricted Boltzmann machine (RBM) network [20] consists of two layers of artificial neurons, one visible layer connected to a hidden layer as shown in Fig. 1. There is no intralayer connection between the neurons. The number of neurons in the visible layer is $N_v = 2L$, where L is the number of lattice sites and that in the hidden layer is N_h . The energy function of an RBM is given by

$$E_{\text{RBM}} = - \sum_{i,j} w_{ij} h_i n_j - \sum_j a_j n_j - \sum_i b_i h_i. \quad (2)$$

The hidden variables h_i take values $h_i = \pm 1$. The set $W = \{\mathbf{a}, \mathbf{b}, \mathbf{w}\}$ denotes the set of all the network parameters a_i , b_j , and w_{ij} . Carrying out the summation over the hidden variables, the probability distribution over the set of input values $\{n_1, n_2, \dots, n_{2L}\}$ is given by

$$\Psi_{\text{RBM}}(R, W) = \frac{1}{Z} \sum_{\mathbf{h}} e^{-E_{\text{RBM}}}, \quad (3)$$

where Z is the partition function. The number of parameters in the network can be drastically reduced by using the symmetries of the Hamiltonian. Here we take the hidden variable density to be $\gamma = N_h/N_v = 1$. In this case, it can easily be seen that imposition of lattice translational symmetry leads to a single bias parameter a for the visible units and a parameter b for the hidden units. Also the number of unique elements in the weight matrix w reduces to $2L$. Thus the total number of network parameters becomes $(2L + 2)$ and the probability function reduces to

$$\Psi_{\text{RBM}}(R, W) = \frac{1}{Z} e^{a \sum_i n_i} \prod_i 2 \cosh \left(\sum_j w_{ij} n_j + b \right). \quad (4)$$

B. Convolutional restricted Boltzmann machine network

The convolutional restricted Boltzmann machine (CRBM) architecture is shown schematically in Fig. 2. It can be thought of as consisting of three layers with an additional convolutional layer in between the visible and the hidden

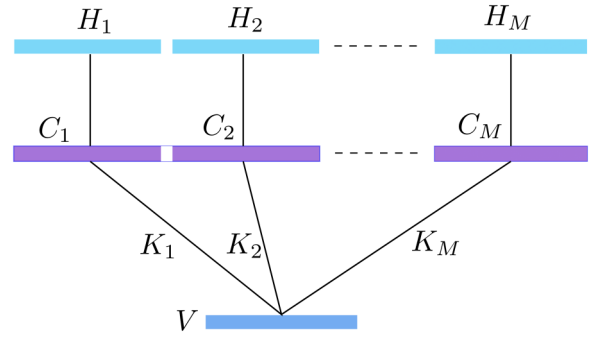


FIG. 2. Schematic diagram of a CRBM network. The visible layer (V) contains $N_v = 2L$ neurons as in RBM. The hidden layer is enlarged compared with RBM and consists of M blocks H_1, H_2, \dots, H_M , each containing N_v neurons. There is a convolutional layer in between which also consists of M blocks C_1, C_2, \dots, C_M . The m th block applies a convolutional filter with kernel K_m to the visible layer and generates an output which is in the form of N_v output neurons comprising the C_m block. There are one-to-one connections between the neurons in the C_m and H_m blocks.

layers [50,51]. Since the underlying lattice is two dimensional (2D), it is necessary to consider layers also to be 2D arrays of neurons instead of the linear arrangement of Fig. 1. The visible layer again contain $N_v = 2L$ neurons, like in the RBM. But the hidden layer (H layer) in the CRBM is enlarged to make it into M blocks H_1, H_2, \dots, H_M , each block containing $N_h = N_v$ neurons. The middle convolutional layer (C layer) also consists of M blocks C_1, C_2, \dots, C_M . The input layer, the blocks' C_m, H_m are all taken to be $2P \times P$ arrays of neurons, where $P = \sqrt{L}$. The m th block applies a convolution filter with kernel K_m to the input layer and produces a result which is in the form of N_v number of convolutional output neurons ($2P \times P$ array) comprising the C_m block. The convolutional output blocks are connected directly to the hidden layer blocks. That is, the i th neuron in m th convolutional block is connected only to the i th neuron of the m th hidden layer block and not to any other hidden unit. Thus, there is a one-to-one connection between the neurons in the blocks C_m and H_m , with a total of N_v connections between the two sublayers. Therefore for $M \ll L$, the total number of connections in the CRBM is much less compared with that in the RBM, making the CRBM representation much more efficient in comparison. Next, consider the convolutional operation by the m th block (Fig. 3). The convolutional filter in the block is defined by its kernel K_m which is a matrix of $D \times D$ parameters ($D \leq P$). Action of the filter on a $D \times D$ window of the visible layer is given by the generalized dot product $K_m \odot V_k$, where V_k is the matrix formed by the input values given to the neurons in this window. This is shown schematically in Fig. 3. We slide the filter with a stride of one step along both the directions to cover the whole of the visible layer. This creates N_v number of windows of the visible layer and hence N_v number of convolutional outputs $K_m \odot V_k$, $k = 1, 2, \dots, N_v$. Denoting the i th hidden variable in the m th block by h_{mi} , the joint energy function in the CRBM is given by

$$E_{\text{CRBM}} = - \sum_{m,k} h_{mk} (K_m \odot V_k) - a \sum_j n_j - \sum_{mi} b_m h_{mi}. \quad (5)$$

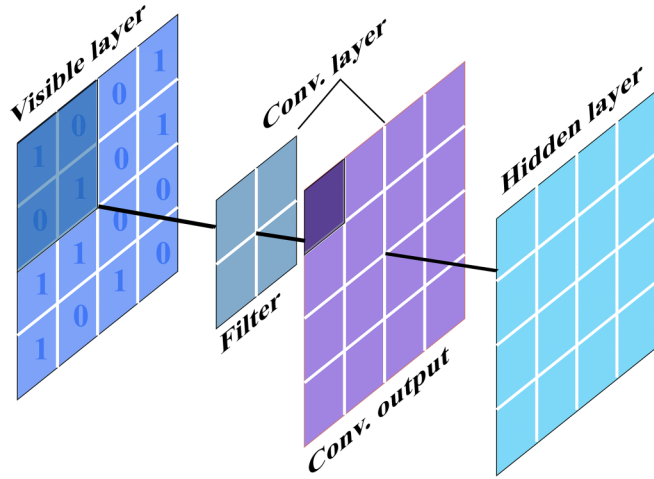


FIG. 3. Schematic diagram showing the convolutional operation by one of the C blocks in Fig. 2. The convolutional layer slides a filter over the visible layer with a stride of one. The operation generates the convolutional output layer which is of the same dimension as the input layer.

It may be mentioned that, by construction, CRBM conserves the lattice translational symmetry imposed in the corresponding RBM. The probability distribution over the visible variables in CRBM is given by

$$\begin{aligned} \Psi_{\text{CRBM}} &= \frac{1}{Z} \sum_{\mathbf{h}} e^{-E_{\text{CRBM}}} \\ &= \frac{1}{Z} e^{a \sum_j n_j} \prod_{mk} 2 \cosh(K_m \odot V_k + b_m), \end{aligned} \quad (6)$$

where Z is a normalization constant. The total number of parameters in the CRBM is $M(2D^2 + 1)$. This number depends only upon the two network structural parameters M and D and not upon the lattice size L . Therefore the number of variational parameters in the CRBM wave function does not grow directly with the lattice size, which is a big advantage in the optimization process. In practice, the parameters M and D are determined by tuning its values so as to obtain the best variational energy. The lattice size might affect these values somewhat, but the number of variational parameters is still expected to be much less than that in the corresponding RBM wave function.

C. Convolutional restricted Boltzmann machine correlated wave function

The CRBM correlated wave function that we consider here is given by

$$|\Psi_{\text{var}}\rangle = \mathcal{P}_{\text{CRBM}} |\text{BCS}\rangle_N, \quad (7)$$

where $|\text{BCS}\rangle_N$ is the ground state (with fixed number of particles) of the following mean-field Hamiltonian:

$$\mathcal{H}_{MF} = \sum_{\mathbf{k}\sigma} \varepsilon_{\mathbf{k}} c_{\mathbf{k}\sigma}^\dagger c_{\mathbf{k}\sigma} - \sum_{\mathbf{k}} (\Delta_{\mathbf{k}} c_{\mathbf{k}\uparrow}^\dagger c_{-\mathbf{k}\downarrow}^\dagger + \text{H.c.}). \quad (8)$$

Here $\varepsilon_{\mathbf{k}} = -2t(\cos k_x + \cos k_y) + 4t' \cos k_x \cos k_y - \mu$, μ being the chemical potential. We take superconducting pairing

amplitude $\Delta_{\mathbf{k}}$ to be of $d_{x^2-y^2}$ -wave (d -wave) symmetry with $\Delta_{\mathbf{k}} = \Delta_{SC}(\cos k_x - \cos k_y)$, where Δ_{SC} is the superconducting (SC) gap parameter. The quantities Δ_{SC} and μ are the variational parameters in the one-body part of the wave function. We consider the wave function in fixed particle number ($2N$) representation with equal number of up and down spins. In terms of the real-space (Wannier) basis, $|\text{BCS}\rangle_N$ can be expressed as

$$\begin{aligned} |\text{BCS}\rangle_N &= \sum_{n_1, n_2, \dots, n_{2L}} \Psi_{\text{BCS}}(n_1, n_2, \dots, n_{2L}) \\ &\quad \times (c_{1\uparrow}^\dagger)^{n_1} \dots (c_{L\uparrow}^\dagger)^{n_L} (c_{1\downarrow}^\dagger)^{n_{L+1}} \dots (c_{L\downarrow}^\dagger)^{n_{2L}} |0\rangle \\ &= \sum_R \Psi_{\text{BCS}}(R) |R\rangle. \end{aligned} \quad (9)$$

Here n_i are the occupation numbers which can take the value zero or one. L is the number of lattice sites. The summation is over the set of values $\{n_1, \dots, n_{2L}\} \equiv R$ subject to constraint $\sum_{i=1}^L n_i = \sum_{i=L+1}^{2L} n_i = N$. The amplitudes $\Psi_{\text{BCS}}(R)$ are the determinantal coefficients corresponding to the electronic configurations. The action of $\mathcal{P}_{\text{CRBM}}$ is given by

$$|\Psi_{\text{var}}\rangle = \mathcal{P}_{\text{CRBM}} |\Phi\rangle = \sum_R \Psi_{\text{CRBM}}(R) \Psi_{\text{BCS}}(R) |R\rangle, \quad (10)$$

where $\Psi_{\text{CRBM}}(R)$ is the output [Eq. (6)] of the CRBM network for a given set of input values $R = \{n_1, \dots, n_{2L}\}$. The variational parameters in the wave function consists of the network parameters plus the parameters in the mean-field part of the wave function.

D. Variational Monte Carlo

Having constructed the variational wave function, we use the variational Monte Carlo (VMC) method [4–6] to compute the variational energy,

$$E_{\text{var}}(\boldsymbol{\alpha}) = \frac{\langle \Psi_{\text{var}} | \mathcal{H} | \Psi_{\text{var}} \rangle}{\langle \Psi_{\text{var}} | \Psi_{\text{var}} \rangle}, \quad (11)$$

and minimize it with respect to the set of variational parameters $\boldsymbol{\alpha}$, which consists of the weight and bias parameters of the neural network and the parameters in the mean-field wave function. We use the stochastic reconfiguration (SR) technique [5,6] for optimization which generally works all even for large number of variational parameters. In this method, the variational parameters $\boldsymbol{\alpha}$ are updated as $\boldsymbol{\gamma} = \boldsymbol{\alpha} - \Delta t S^{-1} \mathbf{g}$, where $\mathbf{g} = \nabla_{\boldsymbol{\alpha}} E_{\text{var}}$ is the energy gradient. S is the overlap matrix with the matrix elements given by $S_{kl} = \langle \Psi_{\alpha_k} | \Psi_{\alpha_l} \rangle$, $|\Psi_{\alpha_k}\rangle = \frac{\partial}{\partial \alpha_k} |\Psi_{\boldsymbol{\alpha}}\rangle$. In the VMC simulations, typically we take $\approx 10^5$ measuring steps after warming up the system for $\approx 10^3$ steps. Each MC step consists of L number of MC moves that include both the hopping and exchange moves, as mentioned before. The number of variational parameters in the CRBM wave function depends on the two network structural parameters M and D and is independent of the lattice size. For the values of M and D considered here, the number of variational parameters becomes of the order of 150. The optimization step even with the SR method sometime does need large number of iterations to converge which creates a bottleneck in the computations.

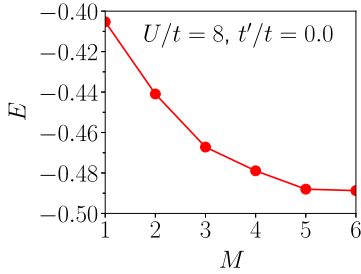


FIG. 4. Energy obtained by repeating optimizations for different values of the CRBM parameter M . The energy reaches a saturation value at $M \approx 5$. The value of the parameter D is four. Model parameters are $U/t = 8$ and $t'/t = 0$.

III. RESULTS

We consider the Hamiltonian on a square lattice of size 10×10 with $L = 100$ sites, and a band filling of one particle per site (half filling). We consider two values of the next-nearest hopping parameter t' , e.g., $t'/t = 0$ and $t'/t = 0.5$. The nonzero value t'/t brings in frustration in the antiferromagnetic order expected at half filling. We study the model as a function of Hubbard onsite interaction U/t . In the results below, all the energy values quoted are energy per site and in units of t .

Before going ahead with the calculations, we need to determine the optimal configuration of the CRBM network. It has two crucial structural parameters—the dimension D of the convolutional kernel and the number of convolution blocks M . In principle, D can vary from one to L . The convolution can be interpreted as a “feature extraction” operation [50]. A value $D = 1$ implies a trivial operation while $D = L$ implies flattening of all features. Here we take $D = 4$ which we find to be an optimal value in terms of performance and efficiency. Regarding value of M , we checked the energy obtained by repeating the optimizations for different values of M . An example plot is shown in Fig. 4. It shows that at $U/t = 8$, the best energy is obtained for a minimum M value of five. In fact, the optimal value of M depends on the value of U . It is smaller for smaller U . Therefore, a value of five works well for the range of U/t considered here and hence we set $M = 5$ for the rest of the calculations.

We optimize the CRBM wave function defined in Eq. (10) by minimizing the corresponding variational energy for a range of model parameter values. For comparison, we also calculate the energies of four other variational wave functions. These are (i) $|\Psi_{GW}\rangle = \mathcal{P}_G|\text{BCS}\rangle_N$ (GW), (ii) $|\Psi_{GW+DH}\rangle = \mathcal{P}_G\mathcal{P}_{DH}|\text{BCS}\rangle_N$ (GW + DH), (iii) $|\Psi_{\text{Jastrow}}\rangle = \mathcal{P}_J|\text{BCS}\rangle_N$ (Jastrow), and (iv) $|\Psi_{\text{RBM}}\rangle = \mathcal{P}_{\text{RBM}}|\text{BCS}\rangle_N$ (RBM), where the projection operators are as defined above. In $|\Psi_{\text{RBM}}\rangle$, we use an RBM network as the correlator. The comparison of energies of these wave functions are shown in Fig. 5. It shows that, in the weak-coupling limit, the energies of these WFs are more or less similar to minor differences among them. However, the energies start to differ in the strong-coupling regime. This is clear from Fig. 5(b) where we have plotted the difference $\Delta E = E_X - E_{\text{CRBM}}$, where X stands for the four other wave functions shown in the figure. As the figure shows, ΔE is negative in the intermediate to strong-coupling regime,

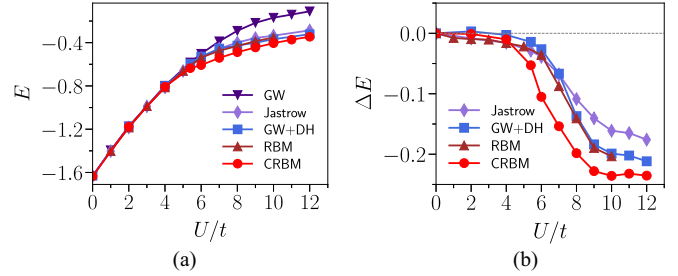


FIG. 5. (a) Energies of the five wave functions described in the text as a function of U/t . (b) The difference $\Delta E = E_X - E_{\text{CRBM}}$, where X stands for the four wave-function names shown in the figure.

indicating that the energy of the GW wave function is highest here. The energies of the GW + DH and RBM wave functions are comparable and lower than that of the Jastrow wave function. The best wave function among the five is the CRBM wave function which yields energies significantly lower than the other four. We also compare the CRBM energies with those for the long-range backflow-Jastrow correlated wave function used in Ref. [48], which was shown to be the most accurate among the Jastrow-type projected wave functions. We find that the CRBM wave function even outperforms the backflow-Jastrow wave function. For example, the backflow WF give energies per site equal to $-0.5961(1)$, $-0.4803(1)$, $-0.4022(1)$, and $-0.3451(1)$ at U/t equal to 6, 8, 10, and 12, respectively. For the same values of U/t , the CRBM wave function give energies per site equal to $-0.6076(2)$, $-0.4882(2)$, $-0.4048(2)$, and $-0.3456(2)$, respectively. These energies are clearly lower than the backflow WF energies. It must be mentioned that the lattice sizes used in these two studies are not the same, and hence the comparison is not strictly rigorous. Still, it gives an idea about how accurate the CRBM wave function is. In Ref. [26], the authors used an RBM correlator in conjunction with a many-variable one-body wave function. The energies of this wave function is actually lower than the CRBM energies, although such a wave function is computationally much more expensive. We also examine the size dependence of the variational energies of all the wave functions listed in Fig. 5(a). We consider two values of U/t , one below and the other above the critical value for Mott transition. The upper panels of Fig. 6 show the energy per site as a function of N , where the lattice size is $L = N \times N$. In each case, the energy of the CRBM wave function is the lowest at all N . The size dependence of the energy for all the WFs becomes small for roughly $N \geq 10$. The lower panels of Fig. 6 show the scaling of the energy as a function of $1/N^3$. It shows that in the Mott state ($U/t = 8$), the CRBM energy scales very accurately as $1/N^3$ as predicted by spin-wave theory [52]. For the other WFs, there are small deviations from this behavior.

Next, we examine the ground-state phase of the model as a function of U/t as described by the CRBM wave function. As mentioned before, we have done calculations for two different values of t' , e.g., $t'/t = 0$ and $t'/t = 0.5$. Although the model has been studied extensively in the past using a variety of methods, several important aspects of its phase diagram including the nature of the zero-temperature Mott transition,

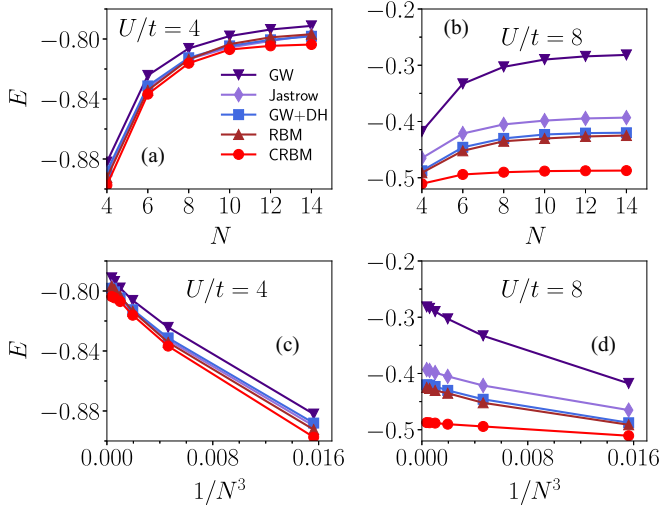


FIG. 6. Size dependence of variational energies of various wave functions shown in the figure at $U/t = 4$ and $U/t = 8$. The upper panels show the energies as a function of N , where the lattice size is $L = N \times N$. The lower panels show the energies as a function of $1/N^3$.

are not yet established unambiguously [2,42,53]. For example, questions exist whether the ground state of the unfrustrated model ($t'/t = 0$) on square lattice is antiferromagnetic (AFM) insulating at any $U/t > 0$, or is it paramagnetic with a finite value of critical interaction U_c/t for Mott metal-insulator transition. What is the nature of Mott insulating state, is it magnetically ordered or a spin liquid? If the unfrustrated model is AFM insulating, is there a critical value of t' beyond which the ground state become paramagnetic metallic? The answers to these questions somewhat vary among different methods. Within the variational theory, the phase diagram of the two-dimensional Hubbard model has been studied by looking at the competition between wave functions with different symmetries. In these wave functions, the one-body part is taken to be either pure BCS type without any magnetic order or an AFM type with explicitly broken spin rotational symmetry. By using the GW-DH projector as the correlator, Yokoyama *et al.* [44] have shown that at $t' = 0$, the lowest-energy state at any $U/t > 0$ is the symmetry-broken one with long-range AFM order and insulating. For $t'/t > 0$, there exists a nonzero value of critical interaction U_c below which the state is paramagnetic metallic (PM). For $U/t > U_c/t$, the state is AFM insulating for small t'/t , but paramagnetic insulating at large t'/t . The transition to the AFM insulating state at $t'/t = 0$ is continuous. It gradually turns first-order at larger t'/t . However, if considered within the nonmagnetic projected BCS wave function only, the state is found to be PM for any t'/t below a critical $U_c/t \neq 0$. In this case, the Mott transition is of first-order nature at any t'/t , and the insulating state is nonmagnetic. In another work, Tocchio *et al.* [47] used variational WFs with backflow correlations in addition to a long-range Jastrow projector. The backflow correlated WFs is much more accurate with lower variational energy compared with only DH or Jastrow-projected WFs. The study also showed that for small U/t and nonzero t'/t , the ground is paramagnetic metallic. It becomes insulating with

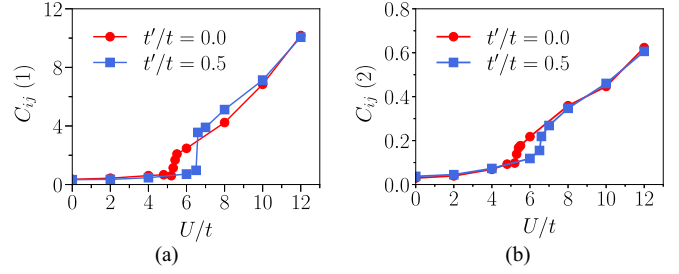


FIG. 7. Doubly-holon correlations at (a) nearest-neighbor and (b) next-nearest-neighbor distances as a function of U/t . Results are shown for two values of t'/t .

a long-range AFM order as U is increased above a critical value. Interestingly, the backflow WF give a region in the phase diagram at large enough values of U/t and t'/t , where the state is an insulating spin-liquid without any long-range magnetic order.

In contrast with the above studies which considered wave functions with different symmetries, here we study the ground state within the single variational wave function. We show that, although no magnetic order is put explicitly into the CRBM + BCS wave function, it spontaneously gives rise to long range AFM order in the insulating state. This is remarkable because, with Gutzwiller-Jastrow type wave functions, one has to introduce explicit symmetry breaking in the wave function in order to obtain a state with strong AFM order. To characterize the ground state, first we compute the doubly-holon (DH) correlation function defined as

$$C_{ij}(r) = \frac{\langle d_i h_j \rangle - \langle d_i \rangle \langle h_j \rangle}{\langle d_i \rangle \langle h_j \rangle}, \quad (12)$$

where $d_i = n_{i\uparrow} n_{i\downarrow}$ and $h_i = (1 - n_{i\uparrow})(1 - n_{i\downarrow})$ are the doubly-holon and holon operators, respectively. The results for the nearest-neighbor (NN) and next-nearest-neighbor (NNN) correlations as a function of U are shown in Fig. 7. It shows that $C_{ij}(r)$ is very close to zero at small U/t . As U/t is increased, it shows a jump at a critical U_c/t and steadily rises after. The NNN values are an order of magnitude smaller than the NN values, indicating the bindings of doubly-holons and holons within short distances from each other. Thus the wave function is able to capture the correct physics of doubly-holon bindings in the strong-coupling regime in spite of it not having any explicit doubly-holon correlation factor. Next, we compute the double occupancy D , defined as

$$D = \frac{1}{N_s} \sum_i n_{i\uparrow} n_{i\downarrow}. \quad (13)$$

It is a crucial quantity that can indicate the presence of Mott transition. The value of D is shown in Fig. 8. Starting from a value of 0.25 at $U/t = 0$, D decreases as U/t is increased. It shows a sudden drop at a critical U_c/t indicating the onset of Mott transition. The jump in the value of D is clearly present at both the values of t' , although it is sharper in the frustrated case. It may be mentioned that, even in the long ranged backflow correlated WF used in previous studies [48], the D at the Mott transition at $t'/t = 0$ shows only a kink, not a jump. We find that the values of critical interaction

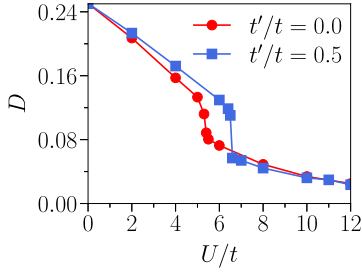


FIG. 8. Double occupancy D as a function of U/t at the two values of t' shown.

are $U_c/t \approx 5.4$ for $t'/t = 0$ and $U_c/t \approx 6.6$ for $t'/t = 0.5$. These values are in roughly in good agreement with previous results [44,47]. The occurrence of the Mott transition can be confirmed directly by looking at the charge gap, which can be estimated from the knowledge of the ground state WF itself. Given the ground state $|\Psi\rangle$, an excited state with momentum \mathbf{q} is given by $n_{\mathbf{q}}|\Psi\rangle$, and the charge gap in the limit $q \rightarrow 0$ for the square lattice can be shown to be [48]

$$E_g = -\frac{1}{4} \left(\lim_{q \rightarrow 0} \frac{|\mathbf{q}|^2}{N(\mathbf{q})} \right) (\mathcal{K}_1 + 2\mathcal{K}_2), \quad (14)$$

where $N(\mathbf{q}) = \langle n_{\mathbf{q}} n_{-\mathbf{q}} \rangle$ is the charge structure factor. \mathcal{K}_1 and \mathcal{K}_2 are the NN and the NNN kinetic energy per site, respectively. The results for E_g are shown in Fig. 9. It confirms that the state below U_c/t is metallic with no charge gap, while above U_c/t it is insulating with a finite charge gap. Next we look at the momentum distribution function, $n(\mathbf{k}) = \langle c_{k\sigma}^\dagger c_{k\sigma} \rangle$. The $n(\mathbf{k})$ values calculated as a function of \mathbf{k} along the symmetry path $\Gamma(0,0)$ - $X(\pi,0)$ - $M(\pi,\pi)$ - $\Gamma(0,0)$ for different values of U/t for the case $t'/t = 0$ are shown in Fig. 10(a). In the metallic state, $n(\mathbf{k})$ has a discontinuity at the Fermi surface, $k = k_F$ in the nodal Γ - M direction. The magnitude of the jump gives the quasiparticle weight Z which roughly corresponds to the inverse effective mass of the quasiparticles [7,44]. We plot the values of Z so determined as a function of U/t in Fig. 10(a). For both the cases of t'/t , Z decreases with increasing U/t and shows a sudden drop at the respective critical interaction U_c/t . Interestingly, Z does not vanish completely in the Mott state for the unfrustrated case at $t'/t = 0$, although it becomes very small. Thus it suggests that the Mott transition in this case takes place via vanishing of spectral weight at the Fermi level rather than via divergence of effective mass. In contrast, Z vanishes completely in the

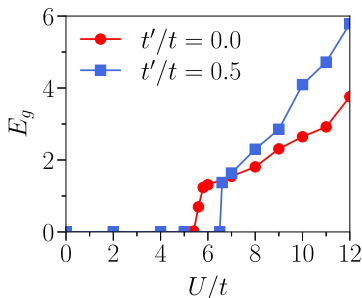


FIG. 9. Charge gap E_g as a function of U/t .

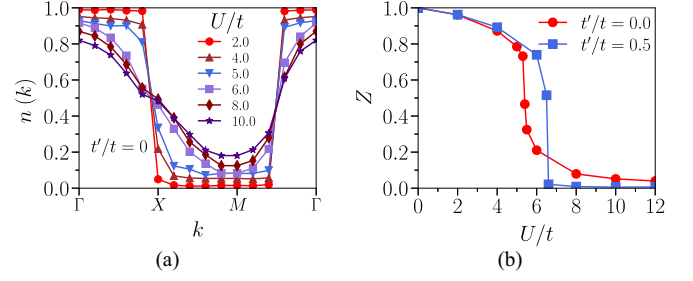


FIG. 10. (a) Momentum distribution at various values of U/t along the symmetry path in the first Brillouin zone ($t'/t = 0$). (b) Quasiparticle weight Z determined from the jump at the Fermi surface, as a function of U/t , for the two cases of t'/t .

Mott state for the $t'/t = 0.5$ case, suggesting divergence of the effective mass in this case. For both the cases, the transition is found to be first order in nature as evinced from discontinuities of various quantities at the critical point. Finally, we look at the magnetic correlations in the CRBM wave function. We calculate the spin structure factor $S(\mathbf{q})$, defined as

$$S(\mathbf{q}) = \frac{1}{L} \sum_{i,j} e^{i\mathbf{q} \cdot (\mathbf{r}_i - \mathbf{r}_j)} \langle S_i^z S_j^z \rangle, \quad (15)$$

where $S_i^z = (n_{i\uparrow} - n_{i\downarrow})$ is the z component of the spin operator at site i . The results for $S(\mathbf{q})$ calculated at various values of U/t are shown in Fig. 11. As the figure shows, $S(\mathbf{q})$ is very small at all \mathbf{q} for $U < U_c$, indicating very weak magnetic correlations in the metallic state. For $U > U_c$, $S(\mathbf{q})$ is very sharply peaked at $\mathbf{q} = (\pi, \pi)$ which indicates onset on long-range AFM correlations as soon as the system enters the Mott state. The nonzero values of t' considered here does not seem have any impact on the AFM correlations. In fact, we find that the sublattice magnetization $m = |S_i^z|$ which is close zero in the metallic phase, jumps to around 0.8 at transition, a value close to the saturation limit. If we compare with results in Ref. [44], the AFM correlations in the insulating state in the GW + DH wave function used in this study is much weaker compared with what is found here. The insets in the figures show $S(\mathbf{q})$ for a small range of $|\mathbf{q}|$. Clearly, in the limit $|\mathbf{q}| \rightarrow 0$, the $S(\mathbf{q}) \propto |\mathbf{q}|$ in the metallic phase suggests an absence of spin gap in this phase. On the other hand,

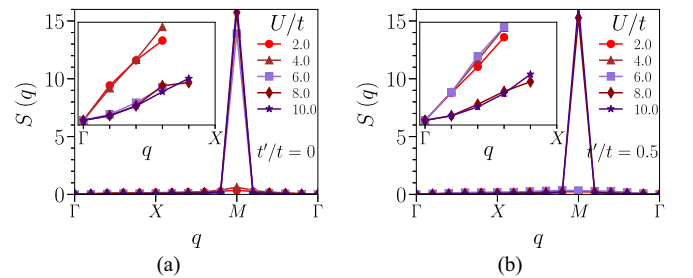


FIG. 11. Spin structure factor $S(\mathbf{q})$ as a function of \mathbf{q} at various values of U/t for the cases (a) $t'/t = 0$ and (b) $t'/t = 0.5$. The insets in each case show $S(\mathbf{q})$ versus \mathbf{q} for small $|\mathbf{q}|$. It shows that in the limit $|\mathbf{q}| \rightarrow 0$, $S(\mathbf{q}) \propto |\mathbf{q}|$ for $U < U_c$ (gapless), while $S(\mathbf{q}) \propto |\mathbf{q}|^2$ for $U > U_c$ (spin gap).

$S(\mathbf{q}) \propto |\mathbf{q}|^2$ for $U > U_c$ suggests that the Mott state is also spin gapped.

IV. CONCLUSION

In summary, we have studied the ground-state phase of the half filled Hubbard model on a square lattice using a variational wave function constructed by applying a convolutional restricted Boltzmann machine (CRBM) neural network as correlator to a mean-field BCS wave function. The number of variational parameters in the wave function does not automatically grow with the lattice size and can be tuned. The wave function is also highly accurate, especially in the strong-coupling limit where it yields variational energies lower than those of the best known Jastrow variational WFs for the model. The picture of Mott metal-insulator transition in the model as described by the CRBM wave function is roughly similar to that obtained by using other variational wave functions [44,47,48], with some interesting differences. Regarding the shortcomings of the CRBM wave function, the results for the energies shows that the it does not necessarily perform

better in the weak-coupling limit. Other more accurate methods strongly suggest that for the unfrustrated model with $t'/t = 0$, there exist short-range AFM fluctuations even in the weak-coupling limit and the ground state in this case is insulating at all $U_c/t > 0$ [2,42,53]. This physics is not captured correctly in the CRBM wave function. This of course can be remedied readily by putting an AFM order manually into the mean-field part of the wave function, although it would be highly desirable to have the correlations generated spontaneously in the same manner as in the Mott insulating state. It is also interesting to study the wave function for a range of t'/t values in order to obtain a full phase diagram as a function of U/t and t'/t . We leave it for a future study.

ACKNOWLEDGMENTS

The authors thank the Science and Engineering Research Board, DST, Govt. of India for financial support under Grant No. CRG/2021/005792. We also acknowledge CHPC, IISER Thiruvananthapuram for computational facilities.

-
- [1] M. Imada, A. Fujimori, and Y. Tokura, Metal-insulator transitions, *Rev. Mod. Phys.* **70**, 1039 (1998).
- [2] J. P. F. LeBlanc, A. E. Antipov, F. Becca, I. W. Bulik, G. K.-L. Chan, C.-M. Chung, Y. Deng, M. Ferrero, T. M. Henderson, C. A. Jiménez-Hoyos, E. Kozik, X.-W. Liu, A. J. Millis, N. V. Prokof'ev, M. Qin, G. E. Scuseria, H. Shi, B. V. Svistunov, L. F. Tocchio, I. S. Tupitsyn, S. R. White, S. Zhang, B.-X. Zheng, Z. Zhu, and E. Gull (Simons Collaboration on the Many-Electron Problem), Solutions of the two-dimensional Hubbard model: Benchmarks and results from a wide range of numerical algorithms, *Phys. Rev. X* **5**, 041041 (2015).
- [3] P. A. Lee, N. Nagaosa, and X.-G. Wen, Doping a Mott insulator: Physics of high-temperature superconductivity, *Rev. Mod. Phys.* **78**, 17 (2006).
- [4] D. Ceperley, G. V. Chester, and M. H. Kalos, Monte Carlo simulation of a many-fermion study, *Phys. Rev. B* **16**, 3081 (1977).
- [5] D. Tahara and M. Imada, Variational Monte Carlo method combined with quantum-number projection and multi-variable optimization, *J. Phys. Soc. Jpn.* **77**, 114701 (2008).
- [6] S. Sorella, Variational Monte Carlo and Markov chains for computational physics, in *Strongly Correlated Systems*, Springer Series in Solid-State Sciences, edited by A. Avella and F. Mancini (Springer, Berlin, Heidelberg, 2013), Vol. 176.
- [7] A. Paramekanti, M. Randeria, and N. Trivedi, High- T_c superconductors: A variational theory of the superconducting state, *Phys. Rev. B* **70**, 054504 (2004).
- [8] H. Shiba and H. Yokoyama, Variational Monte Carlo studies of highly correlated electron systems, in *Proceedings of the Yamada Conference XVIII on Superconductivity in Highly Correlated Fermion Systems*, edited by M. Tachiki, Y. Muto, and S. Maekawa (Elsevier, North-Holland Physics Publishing Division, 1987), pp. 264–267.
- [9] J. Carrasquilla and R. G. Melko, Machine learning phases of matter, *Nat. Phys.* **13**, 431 (2017).
- [10] G. Carleo and M. Troyer, Solving the quantum many-body problem with artificial neural networks, *Science* **355**, 602 (2017).
- [11] E. P. L. van Nieuwenburg, Y.-H. Liu, and S. D. Huber, Learning phase transitions by confusion, *Nat. Phys.* **13**, 435 (2017).
- [12] P. Broecker, J. Carrasquilla, R. G. Melko, and S. Trebst, Machine learning quantum phases of matter beyond the fermion sign problem, *Sci. Rep.* **7**, 8823 (2017).
- [13] K. Ch'ng, J. Carrasquilla, R. G. Melko, and E. Khatami, Machine learning phases of strongly correlated fermions, *Phys. Rev. X* **7**, 031038 (2017).
- [14] D.-L. Deng, X. Li, and S. Das Sarma, Quantum entanglement in neural network states, *Phys. Rev. X* **7**, 021021 (2017).
- [15] G. Carleo, I. Cirac, K. Cranmer, L. Daudet, M. Schuld, N. Tishby, L. Vogt-Maranto, and L. Zdeborová, Machine learning and the physical sciences, *Rev. Mod. Phys.* **91**, 045002 (2019).
- [16] J. Carrasquilla, Machine learning for quantum matter, *Adv. Phys.: X* **5**, 1797528 (2020).
- [17] R. G. Melko, G. Carleo, J. Carrasquilla, and J. I. Cirac, Restricted Boltzmann machines in quantum physics, *Nat. Phys.* **15**, 887 (2019).
- [18] J. Carrasquilla and G. Torlai, How to use neural networks to investigate quantum many-body physics, *PRX Quantum* **2**, 040201 (2021).
- [19] G. Torlai, G. Mazzola, J. Carrasquilla, M. Troyer, R. Melko, and G. Carleo, Neural-network quantum state tomography, *Nat. Phys.* **14**, 447 (2018).
- [20] G. Carleo, Y. Nomura, and M. Imada, Constructing exact representations of quantum many-body systems with deep neural networks, *Nat. Commun.* **9**, 5322 (2018).

- [21] K. Choo, G. Carleo, N. Regnault, and T. Neupert, Symmetries and many-body excitations with neural-network quantum states, *Phys. Rev. Lett.* **121**, 167204 (2018).
- [22] S. Lu, X. Gao, and L.-M. Duan, Efficient representation of topologically ordered states with restricted Boltzmann machines, *Phys. Rev. B* **99**, 155136 (2019).
- [23] I. Glasser, N. Pancotti, M. August, I. D. Rodriguez, and J. I. Cirac, Neural-network quantum states, string-bond states, and chiral topological states, *Phys. Rev. X* **8**, 011006 (2018).
- [24] L. Zhang and Z.-Y. Weng, Sign structure, electron fractionalization, and emergent gauge description of the Hubbard model, *Phys. Rev. B* **90**, 165120 (2014).
- [25] Z. Cai and J. Liu, Approximating quantum many-body wave functions using artificial neural networks, *Phys. Rev. B* **97**, 035116 (2018).
- [26] Y. Nomura, A. S. Darmawan, Y. Yamaji, and M. Imada, Restricted Boltzmann machine learning for solving strongly correlated quantum systems, *Phys. Rev. B* **96**, 205152 (2017).
- [27] K. Inui, Y. Kato, and Y. Motome, Determinant-free fermionic wave function using feed-forward neural networks, *Phys. Rev. Res.* **3**, 043126 (2021).
- [28] D. Luo and B. K. Clark, Backflow transformations via neural networks for quantum many-body wave functions, *Phys. Rev. Lett.* **122**, 226401 (2019).
- [29] D. Pfau, J. S. Spencer, A. G. D. G. Matthews, and W. M. C. Foulkes, *Ab initio* solution of the many-electron Schrödinger equation with deep neural networks, *Phys. Rev. Res.* **2**, 033429 (2020).
- [30] J. R. Moreno, G. Carleo, A. Georges, and J. Stokes, Fermionic wave functions from neural-network constrained hidden states, *Proc. Natl. Acad. Sci. USA* **119**, e2122059119 (2022).
- [31] N. F. Mott, Metal-insulator transition, *Rev. Mod. Phys.* **40**, 677 (1968).
- [32] J. Orenstein and A. J. Millis, Advances in the physics of high-temperature superconductivity, *Science* **288**, 468 (2000).
- [33] A. Georges, G. Kotliar, W. Krauth, and M. J. Rozenberg, Dynamical mean-field theory of strongly correlated fermion systems and the limit of infinite dimensions, *Rev. Mod. Phys.* **68**, 13 (1996).
- [34] X. Y. Zhang, M. J. Rozenberg, and G. Kotliar, Mott transition in the $d = \infty$ Hubbard model at zero temperature, *Phys. Rev. Lett.* **70**, 1666 (1993).
- [35] M. J. Rozenberg, G. Kotliar, and X. Y. Zhang, Mott-Hubbard transition in infinite dimensions. II, *Phys. Rev. B* **49**, 10181 (1994).
- [36] H. Park, K. Haule, and G. Kotliar, Cluster dynamical mean field theory of the Mott transition, *Phys. Rev. Lett.* **101**, 186403 (2008).
- [37] M. J. Rozenberg, R. Chitra, and G. Kotliar, Finite temperature Mott transition in the Hubbard model in infinite dimensions, *Phys. Rev. Lett.* **83**, 3498 (1999).
- [38] R. Bulla, T. A. Costi, and D. Vollhardt, Finite-temperature numerical renormalization group study of the Mott transition, *Phys. Rev. B* **64**, 045103 (2001).
- [39] J. P. Lu, Metal-insulator transitions in degenerate Hubbard models and A_xC_{60} , *Phys. Rev. B* **49**, 5687 (1994).
- [40] M. Ferrero, F. Becca, M. Fabrizio, and M. Capone, Dynamical behavior across the Mott transition of two bands with different bandwidths, *Phys. Rev. B* **72**, 205126 (2005).
- [41] A. Rüegg, M. Indergand, S. Pilgram, and M. Sigrist, Slave-boson mean-field theory of the Mott transition in the two-band Hubbard model, *Eur. Phys. J. B* **48**, 55 (2005).
- [42] A. Mukherjee and S. Lal, Scaling theory for Mott-Hubbard transitions: I. $T = 0$ phase diagram of the 1/2-filled Hubbard model, *New J. Phys.* **22**, 063007 (2020).
- [43] H. Yokoyama and H. Shiba, Variational Monte-Carlo studies of Hubbard model. III. Intersite correlation effects, *J. Phys. Soc. Jpn.* **59**, 3669 (1990).
- [44] H. Yokoyama, M. Ogata, and Y. Tanaka, Mott transitions and d -wave superconductivity in half-filled-band Hubbard model on square lattice with geometric frustration, *J. Phys. Soc. Jpn.* **75**, 114706 (2006).
- [45] M. Capello, F. Becca, M. Fabrizio, S. Sorella, and E. Tosatti, Variational description of Mott insulators, *Phys. Rev. Lett.* **94**, 026406 (2005).
- [46] M. Capello, F. Becca, S. Yunoki, and S. Sorella, Unconventional metal-insulator transition in two dimensions, *Phys. Rev. B* **73**, 245116 (2006).
- [47] L. F. Tocchio, F. Becca, A. Parola, and S. Sorella, Role of backflow correlations for the nonmagnetic phase of the $t-t'$ Hubbard model, *Phys. Rev. B* **78**, 041101(R) (2008).
- [48] L. F. Tocchio, F. Becca, and C. Gros, Backflow correlations in the Hubbard model: An efficient tool for the study of the metal-insulator transition and the large- u limit, *Phys. Rev. B* **83**, 195138 (2011).
- [49] T. A. Kaplan, P. Horsch, and P. Fulde, Close relation between localized-electron magnetism and the paramagnetic wave function of completely itinerant electrons, *Phys. Rev. Lett.* **49**, 889 (1982).
- [50] M. Norouzi, Convolutional Restricted Boltzmann Machines for Feature Learning, Master's thesis, School of Computing Science, Simon Fraser University, 2009.
- [51] D. Alcalde Puente and I. M. Eremin, Convolutional restricted Boltzmann machine aided Monte Carlo: An application to Ising and Kitaev models, *Phys. Rev. B* **102**, 195148 (2020).
- [52] H. Neuberger and T. Ziman, Finite-size effects in Heisenberg antiferromagnets, *Phys. Rev. B* **39**, 2608 (1989).
- [53] T. Schäfer, F. Geles, D. Rost, G. Rohringer, E. Arrigoni, K. Held, N. Blümer, M. Aichhorn, and A. Toschi, Fate of the false Mott-Hubbard transition in two dimensions, *Phys. Rev. B* **91**, 125109 (2015).